THE HIGH-ION CONTENT AND KINEMATICS OF LOW-REDSHIFT LYMAN LIMIT SYSTEMS[*]

Andrew J. Fox[1], Nicolas Lehner[2], Jason Tumlinson[1], J. Christopher Howk[2], Todd M. Tripp[3], J. Xavier Prochaska[4], John M. O'Meara[5], Jessica K. Werk[4], Rongmon Bordoloi[1], Neal Katz[3], Benjamin D. Oppenheimer[6,7], and Romeel Davé[8]

[1] Space Telescope Science Institute, 3700 San Martin Drive, Baltimore, MD 21218, USA; afox@stsci.edu
[2] Department of Physics, University of Notre Dame, 225 Nieuwland Science Hall, Notre Dame, IN 46556, USA
[3] Department of Astronomy, University of Massachusetts, Amherst, MA 01003, USA
[4] UCO/Lick Observatory, University of California, Santa Cruz, CA 95064, USA
[5] Department of Physics, Saint Michael's College, One Winooski Park, Colchester, VT 05439, USA
[6] Leiden Observatory, Leiden University, NL-2300 RA Leiden, The Netherlands
[7] CASA, Department of Astrophysical and Planetary Sciences, University of Colorado, Boulder, CO 80309, USA
[8] University of the Western Cape, Robert Sobukwe Road, Bellville 7535, South Africa

ABSTRACT

We study the high-ion content and kinematics of the circumgalactic medium around low-redshift galaxies using a sample of 23 Lyman limit systems (LLSs) at $0.08 < z < 0.93$ observed with the Cosmic Origins Spectrograph on board the *Hubble Space Telescope*. In Lehner et al., we recently showed that low-z LLSs have a bimodal metallicity distribution. Here we extend that analysis to search for differences between the high-ion and kinematic properties of the metal-poor and metal-rich branches. We find that metal-rich LLSs tend to show higher O vi columns and broader O vi profiles than metal-poor LLSs. The total H i line width (Δv_{90} statistic) in LLSs is not correlated with metallicity, indicating that the H i kinematics alone cannot be used to distinguish inflow from outflow and gas recycling. Among the 17 LLSs with O vi detections, all but two show evidence of kinematic sub-structure, in the form of O vi–H i centroid offsets, multiple components, or both. Using various scenarios for how the metallicities in the high-ion and low-ion phases of each LLS compare, we constrain the ionized hydrogen column in the O vi phase to lie in the range log N(H ii) ~ 17.6–20. The O vi phase of LLSs is a substantial baryon reservoir, with M(high-ion) $\sim 10^{8.5-10.9}$ $(r/150 \text{ kpc})^2$ $M_\odot$, similar to the mass in the low-ion phase. Accounting for the O vi phase approximately doubles the contribution of low-z LLSs to the cosmic baryon budget.

Key words: galaxies: halos – galaxies: kinematics and dynamics – intergalactic medium

Online-only material: color figures

1. INTRODUCTION

The extended ionized halos of galaxies play an important role in the mechanisms that drive galaxy evolution. Loosely referred to as the circumgalactic medium (CGM), these halos serve as reservoirs of baryons and metals, channels through which inflowing and outflowing gas pass, and shields that can hinder the passage of cool gas and quench star formation in the host galaxy. The exchange of matter between galaxies and their CGM is the engine of galaxy growth (Davé et al. 2012). Observationally, the denser regions of the CGM can be seen in the form of Lyman limit systems (LLSs), optically thick quasar absorbers with H i columns between 10^{16} and 10^{19} cm^{-2} (Tytler 1982; Steidel 1990; Ribaudo et al. 2011a; O'Meara et al. 2013; Fumagalli et al. 2013)[9] bridging the gap in H i column between the Lyα forest at N(H i) $\ll 10^{16}$ cm^{-2}, sub-damped Lyα (sub-DLA a.k.a. super-LLS) absorbers at $10^{19} < N$(H i) $< 10^{20.3}$ cm^{-2}, and bona fide DLAs at N(H i) $> 10^{20.3}$ cm^{-2}.

The connection between LLSs and the CGM is based on galaxy detections in the fields of quasars whose spectra contain LLSs (Bergeron 1986; Bergeron et al. 1994; Steidel et al. 1995; Chen & Prochaska 2000; Jenkins et al. 2005; Prochaska et al. 2006, 2011; Lehner et al. 2009; Stocke et al. 2010, 2013;

Ribaudo et al. 2011b; Tumlinson et al. 2011b; Tripp et al. 2011). Observations have established that the CGM can also be probed by strong Lyα forest systems down to $\sim 10^{14.5}$ cm^{-2} (Prochaska et al. 2011; Rudie et al. 2012; Keeney et al. 2013), so LLSs are not the only category of QSO absorber that traces the CGM, but nonetheless they offer a convenient means to identify CGM material. Accurate H i column densities can be obtained in LLSs by measuring the depth of the Lyman break and the strength of the Lyman series absorption lines. Furthermore, the sensitivity of current ultraviolet (UV) data is such that one needs to study LLSs (as opposed to lower column density systems) to be sensitive to *low-metallicity* CGM gas. Simulations reproduce the CGM–LLS connection, predicting that absorbers with N(H i) $\gtrsim 10^{15}$ cm^{-2} trace the CGM of galaxies within impact parameters of $\approx$300 kpc (e.g., Springel & Hernquist 2003; Oppenheimer et al. 2010; Smith et al. 2011; Fumagalli et al. 2011; Sijacki et al. 2012; Vogelsberger et al. 2012; Ford et al. 2013).

In Lehner et al. (2013, hereafter L13), we used a sample of 28 low-redshift ($z < 1$) LLSs observed with the Cosmic Origins Spectrograph (COS) on board the *Hubble Space Telescope* (*HST*) to show that LLSs have a bimodal metallicity distribution, with one peak near 2.5% solar and the other near 50% solar metallicity, and a similar number of absorbers in each branch. A natural interpretation of this result is that the low-metallicity systems trace primitive gas accreting onto galaxies, whereas the high-metallicity systems trace enriched outflowing or recycling gas (L13). If this interpretation is correct, then the covering fractions of inflowing and outflowing/recycling gas in the LLS H i column density range are approximately equal. On the surface, this seems surprising given that the infall of cold gas

[9] LLSs are often defined as extending down to 10^{17} or $10^{17.2}$ cm^{-2}, but in this paper we include "partial" LLSs down to N(H i) $= 10^{16.0}$ cm^{-2}, because these absorbers still create a noticeable spectral break at the Lyman limit.

onto galaxies is found in simulations to be filamentary, generally covering a small solid angle (Ocvirk et al. 2008; Kereš et al. 2009; Faucher-Giguère & Kereš 2011; Fumagalli et al. 2011; Murante et al. 2012; van de Voort & Schaye 2012; Joung et al. 2012b; Shen et al. 2013). However, the inflow covering fraction depends on halo mass (Stewart et al. 2011a), and H I columns may be lower in outflows where the gas is hot and/or highly ionized. Therefore, the full implications of the bimodality of LLS metallicities on the prevalence of inflow and outflow are unclear.

The LLS metallicities reported in L13 were derived from measurements of H I and a range of low- and intermediate-ionization UV metal lines (singly and doubly ionized species), together with photoionization modeling to calculate the ionization corrections. However, these photoionization models generally produce only negligible amounts of O VI, despite the detection of this line in absorption in many LLSs at low redshift ($z < 1$; Chen & Prochaska 2000; Cooksey et al. 2008; Tripp et al. 2008; Lehner et al. 2009; Chen & Mulchaey 2009; Savage et al. 2010; Tumlinson et al. 2011b; Kacprzak et al. 2012; Crighton et al. 2013a), intermediate redshift ($z \approx 1$; Ding et al. 2003; Zonak et al. 2004), and high redshift ($z > 2$; Kirkman & Tytler 1997, 1999; Simcoe et al. 2002, N. Lehner et al., in preparation). O VI absorption is also seen in some sub-DLAs (Fox et al. 2007; Crighton et al. 2013a, 2013b), which trace the CGM just like their lower-N(H I) cousins (Tripp et al. 2005; Battisti et al. 2012). Until now, the relationship between the low-ion and high-ion phases of LLSs has not been explored in a large sample at any redshift.

In this paper we focus on the high-ionization phase of low-z LLSs by surveying absorption in the O VI $\lambda\lambda$1031, 1037 doublet in the L13 sample. We also measure and discuss their kinematic properties. The overall goal is to explore whether the bimodality of LLSs seen in their metallicities is evident in any of their other properties.

Since 113.9 eV is required to ionize O V to O VI (O^{+4} to O^{+5}), O VI is a tracer of either hot, collisionally ionized gas at a few times 10^5 K or warm photoionized plasma at $\sim 10^4$ K subject to a hard (non-stellar) ionizing radiation field. Its properties have been studied in a wide range of interstellar, circumgalactic, and intergalactic environments (see summaries in Heckman et al. 2002; Fox 2011) and are explored in detail in numerical simulations (Oppenheimer & Davé 2009; Cen & Chisari 2011; Tepper-García et al. 2011; Smith et al. 2011). O VI has recently been surveyed in the CGM of 42 low-z galaxies in the COS-Halos sample (Tumlinson et al. 2011a, 2013), with the key result that the O VI column is strongly dependent on the presence or absence of star formation of the host galaxy; our approach here is complementary in that we are using an H I selection rather than a galaxy selection, but we are almost certainly probing the CGM in each case.

This paper is structured as follows. In Section 2 we briefly describe the sample selection. In Section 3 we discuss our measurement procedures. In Section 4 we present results on O VI column density, LLS kinematics, and H II column in the O VI phase. We present a discussion in Section 5 and a summary in Section 6. Throughout this paper we use atomic data for absorption lines from Morton (2003) and Verner et al. (1994) and the solar reference oxygen abundance log (O/H)$_\odot = -3.31$ from Asplund et al. (2009).

2. SAMPLE SELECTION

We began with the L13 sample of 28 LLSs with H I columns between $10^{16.11}$ and $10^{17.00}$ cm^{-2} and redshifts between 0.081

and 0.927, all selected by H I absorption and observed by *HST*. The H I selection (as opposed to an Mg II selection or other metal-line selection) is important for ensuring that no bias toward metal-rich systems is introduced. These systems are drawn from a range of *HST* programs with a variety of science goals, and in all cases the quasars were not targeted to show LLSs. Some sightlines were chosen to *avoid* optically thick absorbers with log N(H I) $\gg 17$. Seven of the systems come from the COS-Halos data set, but these seven do not overlap with the absorption systems with associated galaxies (Tumlinson et al. 2011a; Werk et al. 2013). Measurements of the properties of the low-ion phase of these 28 systems are given in Table 4 of L13. We also make use of supplemental high-resolution ($\approx$6 km s^{-1} FWHM) Keck/HIRES observations covering Mg II $\lambda\lambda$2796, 2803 absorption in 11 of the LLSs and medium-resolution ($\approx$55 km s^{-1} FWHM) Magellan/MagE observations of Mg II in two of the LLSs. These data were reduced as described in Thom et al. (2011) and Werk et al. (2012), respectively.

We then selected those systems with COS data covering the O VI $\lambda\lambda$1031, 1037 doublet, giving 23 LLSs, which is the primary sample for this paper (see Table 1). Twelve of these are in the metal-poor branch ([Z/H] $\leqslant -1$), and 11 are in the metal-rich branch ([Z/H] > -1). All the spectra have a velocity resolution of $\approx$18 km s^{-1} (FWHM) and were taken with either the G130M, G160M, or (in one case) G185M gratings. The data were reduced and normalized following the procedures described in Thom et al. (2011), Meiring et al. (2011), and L13. This includes determining and correcting for wavelength shifts between individual exposures using Galactic interstellar absorption lines. The data were rebinned by three native pixels, to give final spectra with two pixels per 18 km s^{-1} resolution element. Details of the COS instrument are given in Green et al. (2012).

Velocity stacks showing the absorption profiles of H I, a low ion (C II or Si II), an intermediate ion (C III or Si III), and the high-ion O VI are presented for each LLS in the sample in the Appendix. Either C II λ1036, C II λ903.96, or C II λ1334 is chosen to represent the low ions, since these are three of the strongest available lines, although we use Si II λ1020 or Si II λ1260 instead in cases where the C II lines are blended or not covered. C II λ1036 is adopted as the default low-ion line since it lies in between the two members of the O VI $\lambda\lambda$1031, 1037 doublet and hence is unlikely to suffer from zero-point offsets. Likewise, we use C III λ977 as the default intermediate ion, but replace it with Si III λ1206 when C III is saturated or not covered. For H I, we adopt an unsaturated (usually high-order) Lyman series line whenever possible. These stacks allow for comparison of the absorption in each phase of the system and show the data on which our measurements were made. Full velocity-profile plots showing all available metal lines in many (but not all) of these systems are given in L13.

3. MEASUREMENTS

For each LLS, we measure the absorption in each line of interest using the apparent optical depth (AOD) technique of Savage & Sembach (1991). In this technique, the AOD in each pixel is defined as $\tau_a(v) = \ln [F_c(v)/F(v)]$, where $F_c(v)$ is the continuum level and $F(v)$ is the observed flux. The apparent column density in each pixel is $N_a(v) = (m_e c/\pi e^2)[\tau_a(v)/f\lambda] = 3.768 \times 10^{14}\,[\tau_a(v)/f\lambda]$ cm^{-2} (km s^{-1})$^{-1}$, where f is the oscillator strength of the transition and λ is the wavelength in angstroms. Integrating over the profile gives the apparent

Table 1
LLS Column Densities and Kinematic Measurements

Target	Prog.	z_{LLS}	[Z/H]	log N(H I) (cm^{-2})	log N(Mg II) (cm^{-2})	log N(C II) (cm^{-2})	log N(C III) (cm^{-2})	log N(O VI) (cm^{-2})	Δv_{90} (km s^{-1}) H I	Mg II	C II	C III	O VI	δv_0 (km s^{-1}) O VI–H I	C III–H I	C II–H I
PG 1522+101	11741	0.7292	<-2.0	16.66 ± 0.05	<11.71	<13.79	13.33 ± 0.03	13.72 ± 0.07	62	...	...	71	55	8	3	...
J 1435+3604	11598	0.3730	-1.9 ± 0.1	16.65 ± 0.07	11.61 ± 0.09	<14.13#	13.10 ± 0.07	<13.52	49	11	...	66	...	...	19	...
PG 1407+265	11741	0.6828	-1.8 ± 0.3	16.38 ± 0.02	<11.96	<13.17#	13.94 ± 0.01	13.99 ± 0.06	78	...	...	<80	63	-2	6	...
PG 1630+377	11741	0.2740	-1.7 ± 0.1	16.98 ± 0.05	12.19 ± 0.03	<13.66	13.29 ± 0.02*	14.34 ± 0.05	<129	33	...	114*	108	23	13*	...
PG 1216+069	12025	0.2823	<-1.6	16.40 ± 0.05	...	<13.41	13.69 ± 0.01	13.91 ± 0.05	83	...	...	107	128	9	-4	...
J 1619+3342	11598	0.2694	-1.6 ± 0.1	16.48 ± 0.05	11.83 ± 0.09	<13.60	12.97 ± 0.03*	13.83 ± 0.08	76	55	...	57*	40	20	9*	...
PKS 0552$-$640	11692	0.3451	<-1.5	16.90 ± 0.08	<12.48	<12.43#	12.33 ± 0.08*	<13.29	58	...	...	45*	...	...	-3*	...
PHL 1377	11741	0.7390	-1.5 ± 0.1	16.72 ± 0.03	11.92 ± 0.08	12.99 ± 0.12	14.12 ± 0.05	13.94 ± 0.11	<89	22	28	<90	67	12	...	...
J 1419+4207	11598	0.4256	-1.4 ± 0.2	16.17 ± 0.06	...	<13.71	13.26 ± 0.07	13.86 ± 0.08	68	...	...	51	67	-28	0	...
J 1435+3604	11598	0.3878	<-1.4	16.18 ± 0.05	...	<13.67	14.02 ± 0.03	14.14 ± 0.06	146	...	...	<145	76	-50	-24	...
J 0943+0531	11598	0.3544	<-1.3	16.11 ± 0.09	...	<14.09	12.98 ± 0.37	<14.06	164	...	...	...	...	...	...	...
SBS 1122+594	11520	0.5581	-1.0 ± 0.1	16.24 ± 0.03	...	<14.13	13.90 ± 0.02	<14.11	215	...	...	238	...	-4	-0	...
HE 0153$-$4520	11541	0.2261	-0.8 ± 0.2	16.61 ± 0.15	...	14.04 ± 0.03	13.45 ± 0.01*	14.17 ± 0.05	<85	...	73	<74*	106	12	-1*	3
PG 1338+416	11741	0.3488	-0.6 ± 0.2	16.30 ± 0.13	12.46 ± 0.04	13.84 ± 0.05	13.17 ± 0.03*	14.51 ± 0.05	93	54	70	60*	89	-4	15*	1
J 1419+4207	11598	0.2889	-0.6 ± 0.1	16.40 ± 0.07	12.56 ± 0.03	14.07 ± 0.09	13.97 ± 0.04	14.53 ± 0.05	143	50	102	<92	101	25	8	-12
PG 1116+215	12038	0.1385	-0.5 ± 0.2	16.20 ± 0.05	...	13.70 ± 0.04	12.68 ± 0.03*	13.85 ± 0.05	<92	...	53	43*	106	-4	-11*	-11
PKS 0637$-$752	11692	0.4685	-0.5 ± 0.1	16.48 ± 0.04	12.63 ± 0.08	13.63 ± 0.03	13.81 ± 0.01	13.66 ± 0.08	61	87	87	102	87	-3	-16	-6
PG 1522+101	11741	0.5185	-0.4 ± 0.1	16.22 ± 0.02	12.28 ± 0.04	13.34 ± 0.05	13.15 ± 0.04	<13.33	57	20	52	51	...	...	16	5
HE 0439$-$5254	11520	0.6153	-0.3 ± 0.1	16.28 ± 0.04	...	13.85 ± 0.07	14.41 ± 0.06	14.87 ± 0.05	163	...	32	<195	177	3	-2	-8
J 1419+4207	11598	0.5346	-0.2 ± 0.2	16.34 ± 0.17	12.68 ± 0.04	<14.14	13.52 ± 0.06	<13.95	54	31	...	58	...	...	9	...
PG 1338+416	11741	0.6865	$+0.1 \pm 0.1$	16.45 ± 0.05	12.93 ± 0.01	14.16 ± 0.04	14.09 ± 0.06	14.76 ± 0.05	92	<45	75	<86	94	51	31	-7
PKS 0405$-$123	11508	0.1672	$+0.1 \pm 0.2$	16.45 ± 0.05	...	14.22 ± 0.01	13.26 ± 0.01*	14.59 ± 0.05	<127	...	77	93*	177	2	9*	-2
PG 1206+459	11741†	0.9270	$+0.3 \pm 0.1$	17.00 ± 0.10	...	14.94 ± 0.08	14.74 ± 0.09	>15.19	<345	...	<413	<533	<500	-1	...	2

Notes. The redshift z_{LLS}, metallicity [Z/H], and H I column N(H I) of each LLS are taken from L13. All other entries are new measurements. The systems are presented in order of increasing [Z/H]. Prog. refers to the *HST* Program ID of the data used. The errors on the velocity widths Δv_{90} and velocity centroid offsets δv_0 are each ≈ 10 km s^{-1}. No entry is given for Δv_{90} or δv_0 if the relevant line is undetected. For saturated lines, upper limits on Δv_{90} are given. The O VI columns are derived from $\lambda 1031$ unless saturated or blended, in which case $\lambda 1037$ is used. The symbol # indicates that Si II ($\lambda 1020$ or $\lambda 1260$) was used as a proxy for C II. The symbol * indicates that Si III $\lambda 1206$ was used as a proxy for C III $\lambda 977$. The symbol † indicates that COS data from *HST* program 12466 were also used.

column density, $N_a = \int_{v_{min}}^{v_{max}} N_a(v)dv$, where v_{min} and v_{max} define the velocity range of absorption.

Apparent column density profiles for each system in the sample are given in the Appendix. In each LLS we fit Gaussian components to the strongest absorption feature in the H I, C II, C III or Si III, and O VI profiles and measure the velocity centroid offsets δv_0(O VI–H I), δv_0(C III–H I), and δv_0(C II–H I). We note that a large centroid offset δv_0(O VI–H I) does not necessarily indicate that the H I and O VI phases are unrelated; it can also indicate multi-component absorbers with H I/O VI ratios that vary from component to component. Nonetheless, the statistic illustrates whether the bulk of the H I and the bulk of the O VI are offset in velocity, which is a useful indicator of the distribution of the two ions in the absorber.

To verify whether a given offset is significant, one needs to know the reliability of the wavelength solution. The nominal accuracy of the COS wavelength solution is ≈ 15 km s^{-1} (COS Instrument Handbook; Holland et al. 2012). However, we can verify the accuracy on a case-by-case basis by checking the alignment of multiple low-ionization lines from the same system; if the centroids of all the low ions agree to within a few km s^{-1} (which they usually do), but O VI is offset by several times that amount, we can be confident that the offset is real, especially since our default low-ion line is C II $\lambda 1036$, which lies in between the two lines of the O VI $\lambda\lambda 1031, 1037$ doublet and thus offers an excellent reference because it falls in the same regions of the COS detector.

In addition to the velocity centroid offset, we also analyze the total velocity width of absorption Δv_{90}, which we measure for O VI, C II, Mg II, C III or Si III, and H I. This width is defined as the velocity interval containing the central 90% of the integrated AOD in the line (Prochaska & Wolfe 1997). It is measured by integrating each line between v_{min} and v_{max} and finding the difference in velocity between the pixels at which 5% and 95% of the total optical depth has been reached. For each LLS, v_{min} and v_{max} are selected by eye based on assessing the absorption in all ions in the system, but are adjusted in cases of contamination. Δv_{90} has the advantage of being unaffected by the presence of weak satellite components, which do not contribute significantly to the total optical depth in the line, and is thus preferable to the alternative measure of total line width $v_{max}-v_{min}$. However, Δv_{90} does have limitations: for a saturated line, only an upper limit on Δv_{90} can be derived, whereas for a weak line, part of the absorption can be missed in the noise. To deal with these limitations, one approach (see Haehnelt et al. 1998; Ledoux et al. 2006) is to restrict Δv_{90} measurements to lines where $0.1 < F(v)/F_c(v) < 0.6$, and we follow this where possible when choosing between C III and Si III, and when selecting which H I Lyman series line to measure.

The measurements analyzed in this paper are given in Table 1.

4. RESULTS

4.1. O VI Column Densities

O VI absorption is detected at 3σ significance or above in 17 of the 23 LLSs in the sample; among these detections, the mean and standard deviation of log N(O VI) is 14.22 ± 0.44. For comparison, this is lower than the mean O VI column (≈ 14.5) observed in sight lines through the halos of star-forming galaxies (SFGs) at similar redshifts at impact parameters less than 150 kpc (Tumlinson et al. 2011a), and less than the average O VI column seen in sightlines though the Milky Way halo integrated over velocity (≈ 14.4; Wakker et al. 2003; Savage
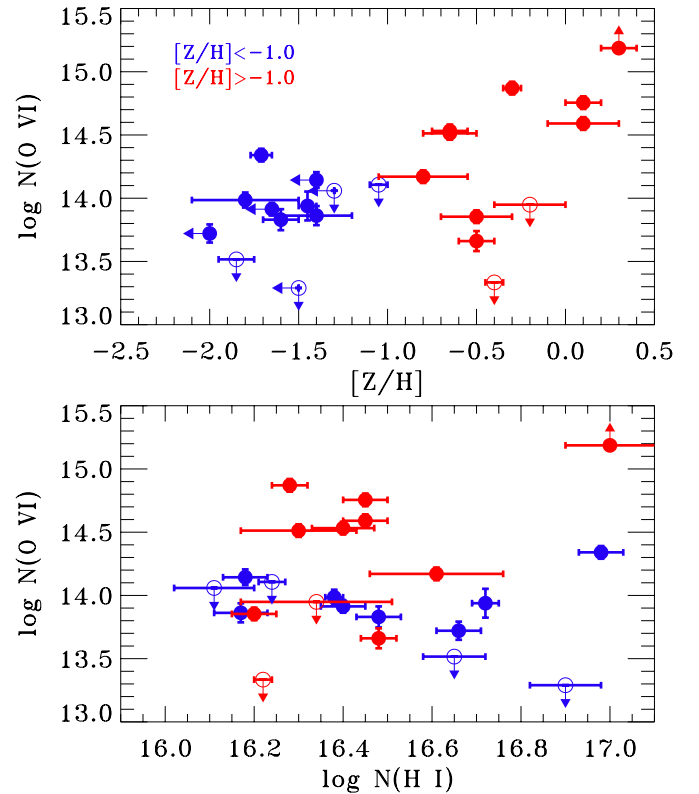

Figure 1. Top panel: O VI column as a function of metallicity for the 23 LLSs in our sample. The metallicities are taken from L13 and are derived from applying photoionization models to the observed low-ion column densities. O VI detections are shown with filled circles and non-detections with open circles and attached upper limit arrows. Lower panel: O VI column vs. H I column. All our systems have $16 < \log N$(H I) < 17 and so fall at the lower end of the LLS column density range. Blue points show low-metallicity LLSs ([Z/H] $\leqslant -1$), and red points show high-metallicity LLSs ([Z/H] > -1).

(A color version of this figure is available in the online journal.)

et al. 2003). In the six LLSs with O VI non-detections, the 3σ upper limits on the O VI column range from log N(O VI) < 13.29 to < 14.14; two of these non-detections lie within the distribution of N(O VI) from the O VI detections.

In the top panel of Figure 1 we plot the O VI column density against metallicity, where the metallicity is derived in the low-ion phase of the LLS by L13. A clear trend is seen in which the high-metallicity LLSs tend to show stronger O VI than the low-metallicity LLSs. All of the 12 metal-poor LLSs ([Z/H] $\leqslant -1$) show weak O VI [log N(O VI) < 14.4], whereas 6 of the 11 metal-rich LLSs ([Z/H] > -1) show strong O VI [log N(O VI) > 14.4]. A Kendall tau correlation test finds evidence for a weak correlation between N(O VI) and [Z/H] (correlation coefficient $= 0.35$) significant at the 97.9% level when treating the upper limits as data points. If we ignore the upper limits and redo the Kendall tau analysis, the significance of the correlation remains similar at 97.6%.

The N(O VI)-metallicity trend can also be seen in the top panel of Figure 2, where we show the distributions of N(O VI) for the [Z/H] $\leqslant -1$ and [Z/H] > -1 sub-samples. A two-sided Kolmogorov–Smirnov (K-S) test rules out the hypothesis that the two distributions are drawn from the same parent population at the 96.4% confidence level (this rises to 97.6% confidence when ignoring the O VI non-detections). In the bottom panel of Figure 2 we display the COS-Halos N(O VI) distribution, showing the O VI columns measured in the CGM
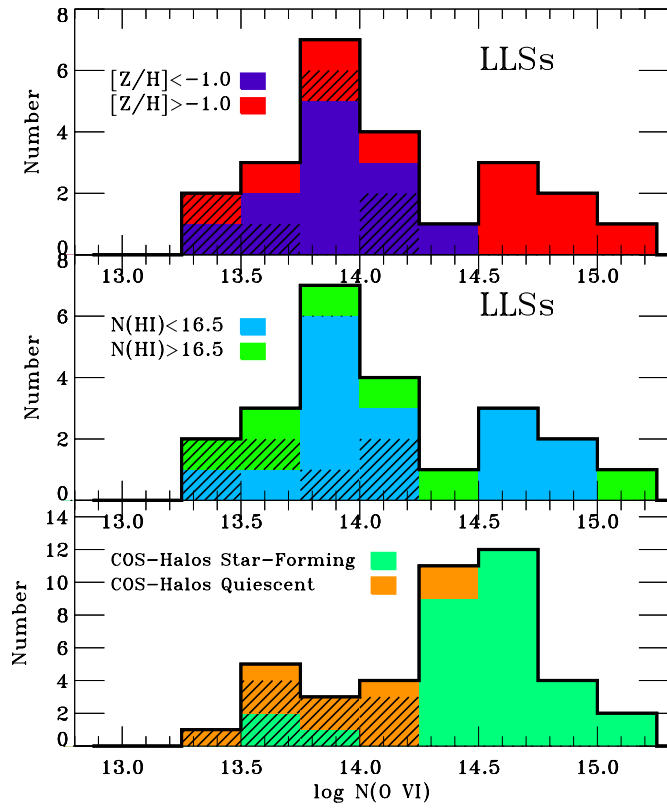
Figure 2. Top panel: histograms of O VI column density in the full LLS sample (black line), low-metallicity sample ([X/H] $\leqslant$ -1.0; blue), and high-metallicity sample ([X/H] $>$ -1.0; red). Upper limits are shown with hatched regions. Middle panel: same as the top panel except the sample is divided into low-H I column (log N(H I) $<$ 16.5; blue) and high-H I column (log N(H I) $>$ 16.5; green) sub-samples. Bottom panel: distributions of N(O VI) in the CGM of the COS-Halos sample of star-forming (green) and quiescent (orange) galaxies (Tumlinson et al. 2011a). Note that many of these COS-Halos absorbers have log N(H I) $<$ 16 and hence are not LLSs.

(A color version of this figure is available in the online journal.)

of SFGs and quiescent galaxies at impact parameters up to 150 kpc (Tumlinson et al. 2011a, 2013), although caution is needed in the comparison since $\approx$70% of these systems have $14.5 < \log N(\text{H I}) < 16.0$ and hence are not LLSs (L13). We note that the metal-rich-LLS distribution overlaps in the range of N(O VI) with the COS-Halos SFG distribution, with a majority of absorbers showing log N(O VI) in the range 14–15 in each case, although the COS-Halos SFG distribution is much more peaked around its maximum value.

In the lower panel of Figure 1, we directly compare the O VI and H I columns in the LLSs. Although there is a cluster of LLSs with strong O VI and log N(H I) lying between 16.2 and 16.5, which creates the visual impression of an anti-correlation, no statistically significant difference in O VI column is seen between the low-H I column [log N(H I) $<$ 16.5] and high-H I column [log N(H I) $>$ 16.5] halves of the samples (see also Figure 2, middle panel).

4.2. LLS Kinematics

In Figure 3, we compare the velocity width Δv_{90} with metallicity, for five species: H I, C II, Mg II, C III or Si III, and O VI. There is no significant difference in the distributions of Δv_{90} between the low-metallicity and high-metallicity sub-samples of LLSs for either H I or C III. For C II, we cannot reliably compare Δv_{90} between the metal-poor and metal-
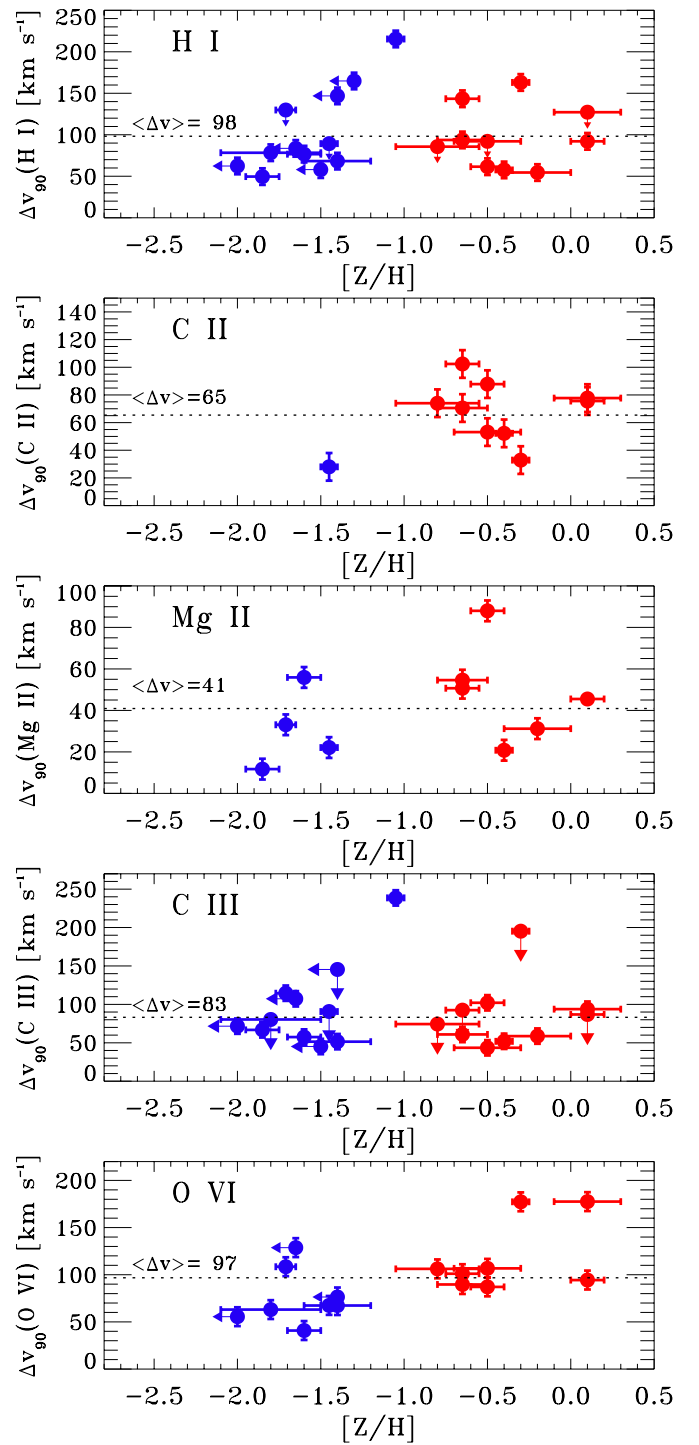
Figure 3. Comparison of velocity width Δv_{90} with metallicity for H I, C II, Mg II, C III, and O VI. Blue points indicate low-metallicity LLSs, and red points indicate high-metallicity LLSs. We use Si III as a proxy for C III in eight cases where it gives a better indication of the intermediate-ion kinematics. Saturated lines give upper limits on Δv_{90}. The $z = 0.927$ LLS toward PG 1206+459 is omitted from this plot; it shows a large velocity spread, covering $\approx$600 km s^{-1}. The sample size varies between ions since Δv_{90} can only be measured if the line is detected. C II is only detected in one of the metal-poor LLSs. In each panel the mean velocity width is annotated and shown with a dotted horizontal line. Note that each panel has a different scale on the y-axis.

(A color version of this figure is available in the online journal.)

rich branches, because there is only one C II detection in the metal-poor branch (no limit on Δv_{90} can be made when a line is not detected). For Mg II, the metal-rich LLSs generally
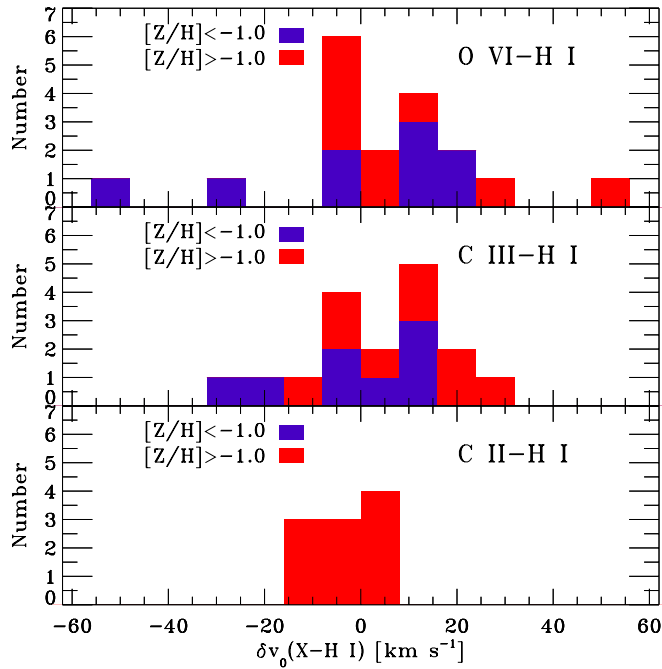
Figure 4. Histograms of velocity centroid offset in the low-metallicity ([X/H] < -1.0; blue) and high-metallicity sub-samples ([X/H] > -1.0; red), for O VI–H I (top), C III–H I (middle), and C II–H I (bottom). This statistic measures the offset between the strongest component of absorption in each ion.
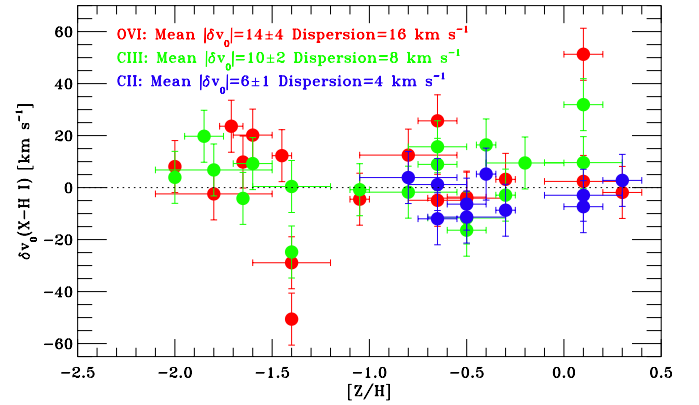(A color version of this figure is available in the online journal.)

Figure 5. Comparison of velocity centroid offset $|\delta v_0|$(X–H I) with metallicity where X is O VI, C III, and C II. Both the mean absolute offset and the dispersion in the absolute offset increase from C II (blue) to C III (green) to O VI (red). These values are annotated on the plot.
(A color version of this figure is available in the online journal.)

appear broader than the metal-poor LLSs, but the sample is small, and there are two metal-rich LLSs with narrow Mg II ($\Delta v_{90} \lesssim 30$ km s^{-1}).

The low-ion velocity widths are in general small (sub-virial), with mean values $\langle \Delta v_{90} \rangle$ of 98 ± 12 km s^{-1} for H I, 65 ± 8 km s^{-1} for C II, 41 ± 8 km s^{-1} for Mg II, and 83 ± 14 km s^{-1} for C III, where the uncertainties quoted are the standard errors of the mean, and where upper limits (from saturated lines) were ignored when calculating these averages. The dispersions around these mean values, $\sigma(\Delta v_{90})$, are 49 km s^{-1} for H I, 24 km s^{-1} for C II, 24 km s^{-1} for Mg II, and 51 km s^{-1} for C III. Aside from the $z = 0.9270$ LLS toward PG 1206+459, for which saturation prevents a measurement of Δv_{90} for most of the lines of interest, the maximum observed Δv_{90} is 215 km s^{-1} for H I, 238 km s^{-1} for C III, and 102 km s^{-1} for C II.

For O VI (Figure 3, bottom panel), the mean Δv_{90}(O VI) $= 97 \pm 10$ km s^{-1} is statistically equal to the mean Δv_{90} for H I, and a factor of ≈ 1.4 higher than the mean Δv_{90} for C III, although there is a large dispersion in Δv_{90} for each line. However, the difference with O VI is that Δv_{90} is a function of metallicity. Three of the four systems with the broadest O VI[10] are three of the four most metal-rich LLSs in the sample (and in these cases, the O VI absorption is substantially broader than the C II). A Kendall tau correlation test finds evidence for a moderate correlation (correlation coefficient $= 0.46$) between Δv_{90}(O VI) and [Z/H] significant at the 99.0% level. A two-sided K-S test rules out the hypothesis that the distributions of Δv_{90}(O VI) in the metal-poor and metal-rich branches are drawn from the same parent population at the 99.3% confidence level.

The other kinematic statistic we analyze is the velocity centroid offset $|\delta v_0|$ between the strongest absorption component seen in various ions. We find that $|\delta v_0|$(O VI–H I) is >10 km s^{-1}

in 8 of the 17 LLSs where O VI is detected, and >20 km s^{-1} in 6 of these systems (Figure 4). For intermediate ions C III or Si III, denoted X III for short, we find that $|\delta v_0|$(X III–H I) is >10 km s^{-1} in 8 of the 20 cases where C III or Si III is detected. As mentioned in Section 3, these centroid offsets provide important observational information on the distribution of the absorbing ions in velocity space in each absorber, but can reflect component structure within the absorber. Large values of $|\delta v_0|$(O VI–H I) indicate that the bulk of the O VI is offset from the bulk of the H I. The O VI–H I centroid offsets distribute similarly for metal-rich and metal-poor LLSs (Figure 4), with offsets extending to ± 50 km s^{-1} around the systemic redshift of the absorber, and with no evidence for asymmetry around zero.

The offsets $|\delta v_0|$(X–H I) where X is O VI, C III, and C II are plotted against LLS metallicity in Figure 5. Across the whole sample, we find that the mean absolute offset $\langle |\delta v_0| \rangle$(X–H I) is 14 ± 4 km s^{-1} for O VI, 10 ± 2 km s^{-1} for C III, and 6 ± 1 km s^{-1} for C II, where the uncertainties quoted are the standard errors of the mean. The dispersion in the centroid offsets $\sigma(|\delta v_0|)$(X–H I) decreases from 15 km s^{-1} for O VI–H I, to 8 km s^{-1} for C III–H I, to 3 km s^{-1} for C II–H I. Therefore, both the mean absolute offset and its dispersion appear to increase with ionization potential from C II to C III to O VI. This can also be seen in the histograms shown in Figure 4.

It is useful to assess whether the line profiles in each LLS are consistent with a single component, i.e., whether the H I and all metal lines can coexist in a single cloud at a single velocity. Of the 23 LLSs in our sample with O VI detections, 12 show multi-component structure (this structure is most visible in C III $\lambda 977$, but is often seen in H I and O VI as well). The remaining five have absorption profiles that are consistent with a single component. Only two absorbers in the sample, the $z = 0.2694$ LLS toward J 1619+3342 and the $z = 0.7292$ LLS toward PG 1522+101, show both a single component *and* a small centroid offset $|\delta v_0|$(O VI–H I) < 10 km s^{-1} (these two are both metal-poor LLSs with very weak O VI). In other words, these are the only two systems where the line profiles allow a solution in which all observed species could arise in a single cloud at a single central velocity (and even in these two, the aligned O VI and H I components could arise in a chance coincidence of distinct clouds).

The overall conclusion from our kinematic analysis, considering the total line widths, the velocity centroid offsets, and the

---

[10] These are the $z = 0.6153$ LLS toward HE 0439–5254, the $z = 0.9270$ LLS toward PG 1206+459, and the $z = 0.1672$ absorber toward PKS 0405–123.

component structure, is that LLS absorption profiles are complex, with differences between the high-ion and low-ion profiles in all but two of the systems in our sample. The O VI profiles show a broader mean Δv_{90} than the low-ion profiles and a larger mean centroid offset from H I than the low ions. In almost half the sample (8 of 17 LLSs) there is a velocity centroid offset $|\delta v_0|$(O VI–H I) > 10 km s^{-1}, indicating that the bulk of the O VI and H I do not coexist in the same regions.

4.3. Ionized Hydrogen Column in O VI Phase

The correlation between O VI column and metallicity reported in Section 4.1 has implications for the ionized hydrogen column density N(high-ion H II) in the O VI phase, which is given by

$$N(\text{high} - \text{ion H II}) = N(\text{O VI})/[f(\text{O VI})(\text{O/H})_{\text{high-ion}}].$$

Here $f(\text{O VI}) \equiv \text{O VI}/\text{O}$ is the O VI ionization fraction and (O/H)$_{\text{high-ion}}$ is the oxygen abundance in the O VI-bearing gas. To evaluate N(high-ion H II) in each LLS, we need to determine the ionization level and metallicity. First, we adopt a common ionization fraction for all systems, using the maximum O VI fraction $f(\text{O VI})_{\text{max}} = 0.2$ permitted under either equilibrium or non-equilibrium collisional ionization models (Sutherland & Dopita 1993; Gnat & Sternberg 2007; Oppenheimer & Schaye 2013), which gives a *minimum* high-ion H II column. To evaluate the metallicity, we consider three scenarios, which cover the plausible range of parameter space:
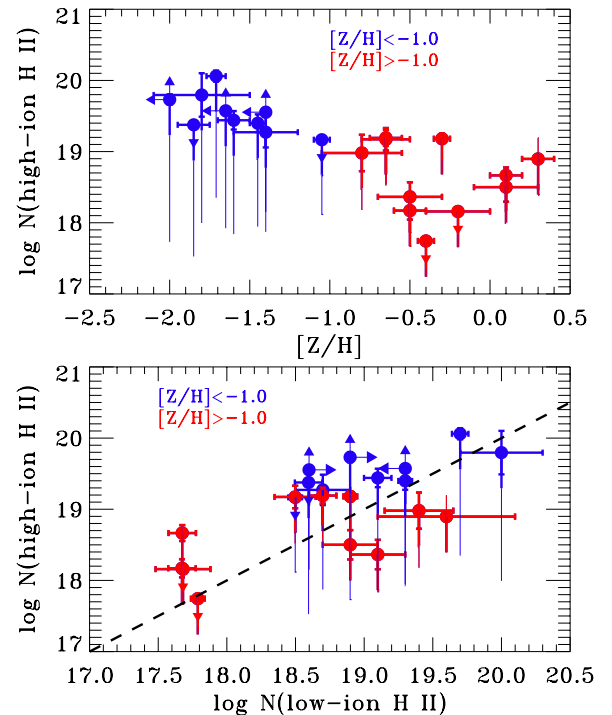
Case 1: the metallicity in the high-ion phase of each LLS is equal to that measured in the low-ion phase. This scenario would apply if the low-ion phase condensed out of the high-ion phase (see Maller & Bullock 2004; Joung et al. 2012a), or conversely if the high-ion phase was heated and evaporated out of the low-ion phase.

Case 2: the metallicity in the high-ion phase of each LLS is 0.5 dex (factor of three) *higher* in the O VI phase than the low-ion phase, as was found observationally for the LLS at $z = 0.2261$ toward HE 0153−4520, discussed in detail in Savage et al. (2011). By decomposing the Lyα absorption profile in this system into narrow (low-ion) and broad (high-ion) components, these authors derived the metal abundance separately in the two phases, finding [X/H]$_{\text{low-ion}} = -0.8^{+0.3}_{-0.2}$ and [O/H]$_{\text{high-ion}} = -0.28^{+0.09}_{-0.08}$, corresponding to a factor of three enhancement in metallicity in the high-ion phase.

Case 3: the O VI phase traces gas with solar metallicity, as might apply if it traced galactic outflows or recycled wind material (e.g., Stinson et al. 2012).

The values of N(high-ion H II) evaluated in these three cases are shown in Figure 6. The data points show the values calculated in case 1, with the downward-pointing "error" bars extended to account for cases 2 and 3. In case 1, log N(high-ion H II) lies in the range $\approx$18–20, whereas in case 3, log N(high-ion H II) lies in the narrower range $\approx$17.6–18.6. In cases 1 and 2, N(high-ion H II) is *anti-correlated* with metallicity, so that the high-metallicity systems show a deficit of high-ion plasma even though they tend to show stronger O VI. In other words, in these scenarios the N(O VI)–metallicity correlation shown in Figure 1 is shallower than would be expected if driven by metallicity alone. However, in case 3, N(high-ion H II) shows much less dependence on [Z/H].

The high-ion H II columns can be directly compared to the low-ion ($\approx 10^4$ K) H II columns derived in each LLS from the *Cloudy* photoionization models of L13. This is shown

Figure 6. Top panel: H II column in the O VI phase (=high-ion H II) as a function of LLS metallicity, assuming that the metallicity in the low-ion and high-ion phases of each LLS are equal (case 1), and that the O VI ionization fraction $f(\text{O VI}) = 0.2$. The thick downward error bars indicate the effect of using a 0.5 dex higher metallicity in the O VI phase (case 2). The thin downward error bars indicate the effect of using a solar metallicity in the O VI phase (case 3). Lower panel: N(high-ion H II) vs. N(low-ion H II), where the values of N(low-ion H II) are taken from the photoionization models of L13. The dashed line shows the relation N(high-ion H II) = N(low-ion H II). Blue and red points show the metal-poor and metal-rich sub-samples. Lower limits on N(high-ion H II) indicate absorbers with upper limits on metallicity. Upper limits on N(high-ion H II) indicate absorbers with no O VI detections.

(A color version of this figure is available in the online journal.)

in the lower panel of Figure 6. The key result here is that the H$^+$ columns in the high-ion and low-ions phases are of similar order, *even when accounting for the possibility that* (O/H)$_{\text{high-ion}} \approx 3(O/H)_{\text{low-ion}}$ as discussed in case 2 above. In addition, the H II columns in the two phases are correlated (in cases 1 and 2), though this is driven by their similar dependence on metallicity, with both being proportional to $1/(Z/H)$. Other examples exist in the literature of LLSs where N(high-ion H II) $> N$ (low-ion H II) (Tripp et al. 2011; Crighton et al. 2013b). Intergalactic absorption-line systems with lower H I columns can also show this property (Meiring et al. 2013).

The magnitude of the baryon reservoir in the various forms of hydrogen in LLSs is shown in Figure 7, where the breakdown of hydrogen column in each LLS into H I, low-ion H II, and high-ion H II is plotted for two of our three metallicity cases. The strength of the green and red bars relative to the blue bars clearly indicates that H I is a trace constituent of LLSs and H II dominates their baryon content, with both low-ion H II and high-ion H II making significant contributions.

5. DISCUSSION

The recent result of L13 that low-redshift LLSs have a bimodal metallicity distribution has placed important constraints on the distribution of gas in the CGM of low-redshift galaxies. In this paper, we have searched for evidence of bimodality in other LLS properties, particularly their kinematics and
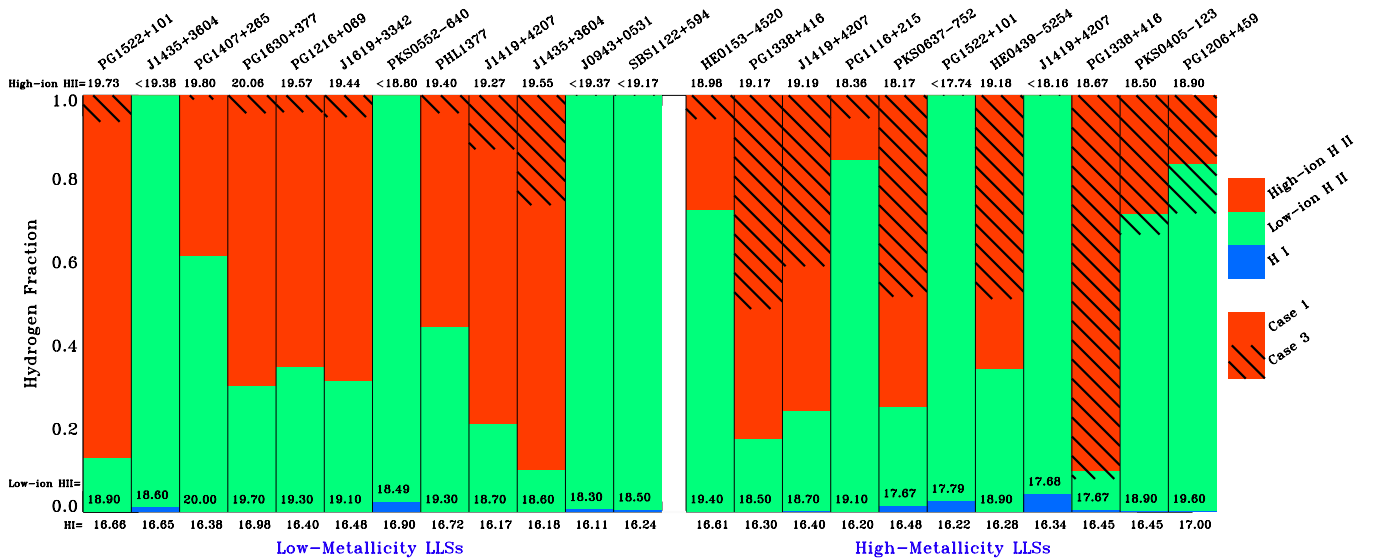
Figure 7. Summary of the hydrogen ionization breakdown in each absorber, illustrating the relative column densities in each phase. Each column represents an LLS, identified at the top, ordered from low to high metallicity. The colored bars represent the fraction of the total hydrogen column residing in the H I, low-ion H II, and high-ion H II phase. The numbers annotated on each bar show the logarithm of the hydrogen column density in that phase. The high-ion H II fractions are shown for two of the metallicity cases described in Section 4.3: case 1 (full red), where the metallicity in the high-ion and low-ion phase of each LLS is the same, and case 3 (hatched red), where the high-ion metallicity is solar (case 2 lies in between). The low-ion H II columns are taken from L13. In most cases, the H I contribution is negligible since the LLSs are so highly ionized, and the blue H I bar is not visible.

(A color version of this figure is available in the online journal.)

high-ion columns. Interestingly, the LLS bimodality is *not* reflected in their bulk H I kinematics or intermediate-ion (C III or Si III) kinematics: the metal-poor and metal-rich LLS branches have similar mean velocity widths Δv_{90} for C III and H I. Given that metal-poor LLSs are thought to trace galactic inflows and metal-rich LLSs trace outflows or recycled material (L13), we find that the H I line widths are not a good way to distinguish inflowing and outflowing gas. Determining the systemic velocities of the LLS host galaxies would allow us to look for H I-galaxy velocity offsets, which are predicted by cold-mode inflow models to be a signature of inflow (Stewart et al. 2011b), although the simulations of Ford et al. (2014) find that H I radial velocity measurements are generally poor at distinguishing inflow and outflow.

If the H I (and C III) velocity width traces the depth of the potential well in which the LLS resides, and hence the mass of the underlying halo (as is thought to be the case for DLAs), our results indicate that the LLS metallicity is independent of the mass. Alternatively, the lack of a metallicity–kinematics correlation (Figure 3) may indicate that the LLS kinematics *do not* probe the halo mass, which would be the case if LLSs are smaller, sub-virial structures with randomly ordered velocity fields that do not fill the potential well of their host halo.

At high redshift ($z > 2$), a clear correlation between Δv_{90}(low ion) and metallicity has been observed in DLAs and sub-DLAs (Ledoux et al. 2006; Prochaska et al. 2008; Dessauges-Zavadsky et al. 2009; Kulkarni et al. 2010; Neeleman et al. 2013). This has been interpreted as an indication of an underlying mass–metallicity relation in the host galaxies (Ledoux et al. 2006). At lower redshift ($z < 1.5$), DLAs show the Δv_{90}(H I)–[Z/H] correlation, but the data for sub-DLAs are inconclusive (Meiring et al. 2009). Our results reinforce the finding that the trend between metallicity and velocity width weakens as one descends in H I column, and they extend this finding from DLAs and sub-DLAs down to the LLS regime.

The LLS bimodality is reflected to some degree in the O VI properties, although instead of a clean N(O VI)–[Z/H] correlation, we see a lack of low-metallicity LLSs with strong O VI; high-metallicity LLSs can have either strong or weak O VI. The O VI line width is correlated with metallicity, with three of the four broadest (and strongest) systems also happening to be three of the four most metal-rich systems in the sample. The O VI in these systems can naturally be interpreted as being produced by galactic outflows, as has been discussed in detail for the $z = 0.937$ absorber toward PG 1206+459 (Tripp et al. 2011).

Our results on the H$^+$ column in the O VI phase of LLSs indicate that a substantial mass of highly ionized gas is present in these absorbers. Given an O VI covering fraction of unity out to 150 kpc around low-z SFGs (Tumlinson et al. 2011a), which we take as indicative of the physical size of the O VI-bearing CGM, the high-ion H II mass can be calculated as $M_{\rm high-ion} = \pi r^2 \mu m_{\rm H} N({\rm high\text{-}ion\ H\,II})$. Using the values of log N(high-ion H II) $\sim$ 17.6–20 we derived in Section 4.3 and a factor $\mu = 1.3$ to account for the mass in helium and metal atoms, we find M(high ion) $\sim 10^{8.5-10.9}(r/150\,{\rm kpc})^2\,M_\odot$. This is a separate reservoir than the mass traced by the low and intermediate ions in LLSs, which is also estimated to be $\sim 10^{9-11}\,M_\odot$ (L13; Werk et al. 2013; J. K. Werk, in preparation). We therefore find that including the O VI-traced phase of LLSs approximately doubles their contribution to the cosmic baryon census, which is still incomplete (Bregman 2007; Shull et al. 2012).

Our claim that the high-ion phase of LLSs is distinct from the low-ion phase is based on the kinematic results presented in Section 4.2, which indicate that all but two of the LLSs have kinematic sub-structure, in the form of velocity centroid offsets between the strongest H I and O VI absorption, multiple components, or both. This result is valid independent of any ionization modeling and follows merely from inspection of the absorption-line profiles. The coexistence of high-ion and low-ion absorption at similar velocities has been noted before in

many LLSs and in Lyα forest absorbers at lower H I column (e.g., Tripp et al. 2008; Wakker & Savage 2009; Howk et al. 2009; Churchill et al. 2012).

A separate line of argument that LLSs are multi-phase (containing regions of differing density and temperature) is that single-phase photoionization models systematically underproduce the observed O VI column densities (Cooksey et al. 2008; Lehner et al. 2009; Tumlinson et al. 2011b; Tripp et al. 2011; Kacprzak et al. 2012; Crighton et al. 2013a, L13) given standard models of the incident ionizing radiation field (the UV background; Haardt & Madau 1996, and later updates). This underproduction of O VI by photoionization models is also the case in the Galactic high-velocity clouds (HVCs; Sembach et al. 2003; Collins et al. 2005; Fox et al. 2005; Ganguly et al. 2005), gaseous objects lying in the low halo of the Milky Way, many of which have H I columns that classify them as LLSs (Fox et al. 2006), although we note that HVCs on average trace gas at lower impact parameters than LLSs (Lehner & Howk 2011; Lehner et al. 2012). In HVCs the favored mechanism for the production of the high ions is in the conductive (Gnat et al. 2010), turbulent (Kwak et al. 2011), or shocked (Hartigan et al. 1987; Dopita & Sutherland 1996) boundary layers between the clouds and a surrounding million-degree corona, because these models can reproduce the kinematics and line strengths of the HVC high-ion absorption profiles, although no single ionization model is able to account for all the high-ion profiles observed in Milky Way halo directions (Wakker et al. 2012; Marasco et al. 2013).

We stress that in the interface picture, the high ions do not directly trace a diffuse 10^6 K corona, but rather the boundary layers where such a corona interacts with embedded cool clouds. The O VI column observed in a sightline through a single interface is independent of the cloud's metallicity (Heckman et al. 2002), because of the physics of radiatively cooling gas: lowering the oxygen abundance lengthens the cooling time, so oxygen atoms stay in the O VI phase for longer, compensating for their lower abundance. In this picture, the variable that leads to the higher O VI columns is a larger number of components along the line of sight.

Alternative models place the O VI in a diffuse, extended hot halo (Mo & Miralda-Escudé 1996; Maller et al. 2003; Stinson et al. 2012; Shen et al. 2013; Ford et al. 2013; Hummels et al. 2013). In simulations, cold accretion (which we argue can be seen in the form of low-metallicity LLSs) dominates in low-mass halos, which do not possess a million-degree halo since their virial temperature is too low. The O VI absorption in such systems arises from winds, mostly on their way out, since there is not much wind re-accretion in low-mass halos (Oppenheimer et al. 2010). On the other hand, high-metallicity LLSs are thought to arise in both low-mass and high-mass halos. In the low-mass case, the O VI would arise from outflows, as for low-metallicity LLSs. In the high-mass case, the O VI could arise from either inflowing or outflowing gas, since high-mass halos play host to more wind re-accretion (Oppenheimer et al. 2010), or from quasi-hydrostatic halo gas that is not participating in inflow or outflow.

We conclude by mentioning the lack of O VI absorption in 5 of the 23 LLSs in our sample, 3 of which have sensitive (constraining) non-detections with log N(O VI) < 13.6. One interpretation of these absorbers is that they trace the CGM of quiescent, red-and-dead galaxies, either with halos too hot for O VI (although this would leave unanswered the question of why such halos frequently show H I) or with no hot halos at all, as opposed to the CGM of SFGs. This would be broadly consistent with recent results on quiescent galaxies, which generally do not show O VI absorption (Tumlinson et al. 2011a) but in ≈40%–50% of cases show strong H I [log N(H I) $\gtrsim$ 16] within 150 kpc (Thom et al. 2012). The similar range of O VI column detected in our LLS sample and in the COS-Halos SFG sample supports (but does not require) this interpretation. However, two of the sensitive O VI non-detections are in metal-poor LLSs, which are expected theoretically to trace low-mass halos, not the halos of massive ellipticals, and hence these two require an alternative explanation.

Follow-up imaging of the host galaxies of the full sample of LLSs discussed here will allow us to relate the O VI properties to the galaxy properties. In particular, such imaging would allow us to compare the O VI with the orientation of the host galaxy disk, and hence look for evidence that O VI-bearing outflows preferentially occur along the minor axis of the galaxy, as is the case for Mg II absorbers (Kacprzak et al. 2011; Bouché et al. 2012; Bordoloi et al. 2013). It would also allow us to investigate whether r = 150 kpc is a suitable impact parameter to use for LLS host galaxies; indeed, 11 of the 23 LLSs already have a candidate host galaxy identified within ≈120 kpc (L13).

6. SUMMARY

We have studied the high-ionization phase and kinematics of the CGM around low-z galaxies by surveying O VI absorption in a sample of 23 low-z ($0.08 < z < 0.93$) LLSs observed with *HST*/COS. The data are supplemented in 11 cases by Keck/HIRES spectroscopy, and in two cases by Magellan/MagE spectroscopy, to provide coverage of Mg II. This has allowed us to place empirical constraints on the properties of the high-ion phase of the CGM and its relation to the low-ion phase, and to search for bimodality in other LLS properties following the finding of L13 that LLSs have a bimodal metallicity distribution. Our key results are as follows:

1. Seventeen of the 23 LLSs show O VI detections. Among these, the mean log N(O VI) is 14.22 ± 0.44. We find a moderate trend (97.6% confidence) in which metal-rich ([Z/H] > −1) LLSs show higher O VI columns than metal-poor ([Z/H] < −1) LLSs. Metal-poor LLSs only show weak O VI; metal-strong LLSs can show strong or weak O VI. There is no correlation between the LLS O VI column and H I column.

2. Among the 17 systems with O VI detections, all but two show evidence of kinematic sub-structure, in the form of velocity centroid offsets between the strongest components of O VI and H I absorption of more than 10 km s^{-1}, multiple components, or both. The centroid offsets extend up to ±50 km s^{-1} around the systemic redshift and are not a function of LLS metallicity. The mean absolute centroid offset from H I increases from C II to C III to O VI: $\langle|\delta v_0|\rangle$(C II–H I) = 6 ± 1 km s^{-1}, $\langle|\delta v_0|\rangle$(C III–H I) = 10 ± 2 km s^{-1}, and $\langle|\delta v_0|\rangle$(O VI–H I) = 14 ± 4 km s^{-1}. Thus, we find a tentative trend in which the higher the ionization state, the larger the average velocity offset from the H I of the strongest absorption component.

3. We compare the measured velocity widths Δv_{90} for H I, C II, Mg II, C III, and O VI with metallicity. We find no significant difference in the distribution of Δv_{90}(C III) and Δv_{90}(H I) between the low-metallicity and high-metallicity sub-samples. *Thus, the bimodality of LLSs in their metallicities is not reflected in their* H I *kinematics or their*
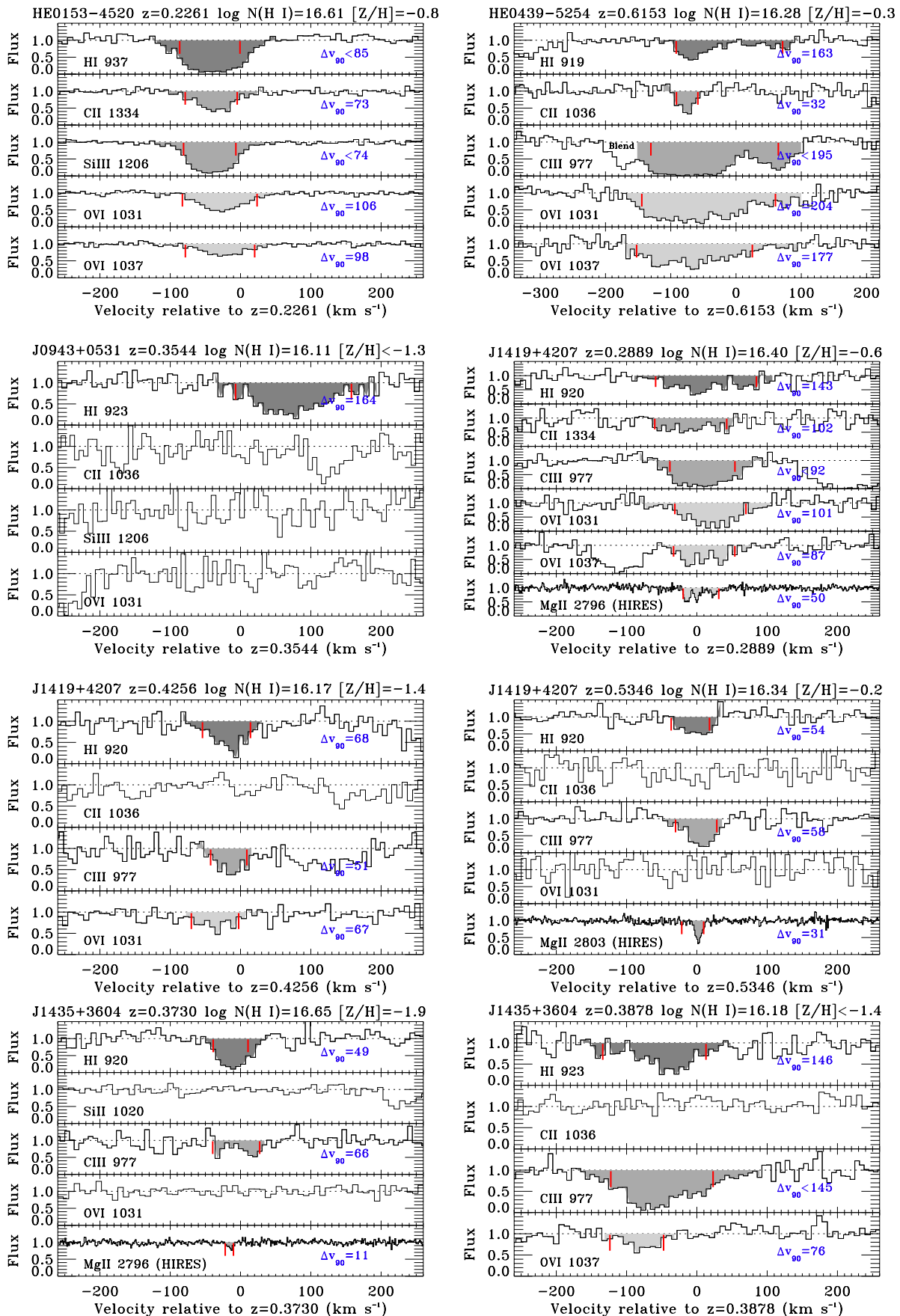
Figure 8. Normalized flux profiles for each LLS in the sample.

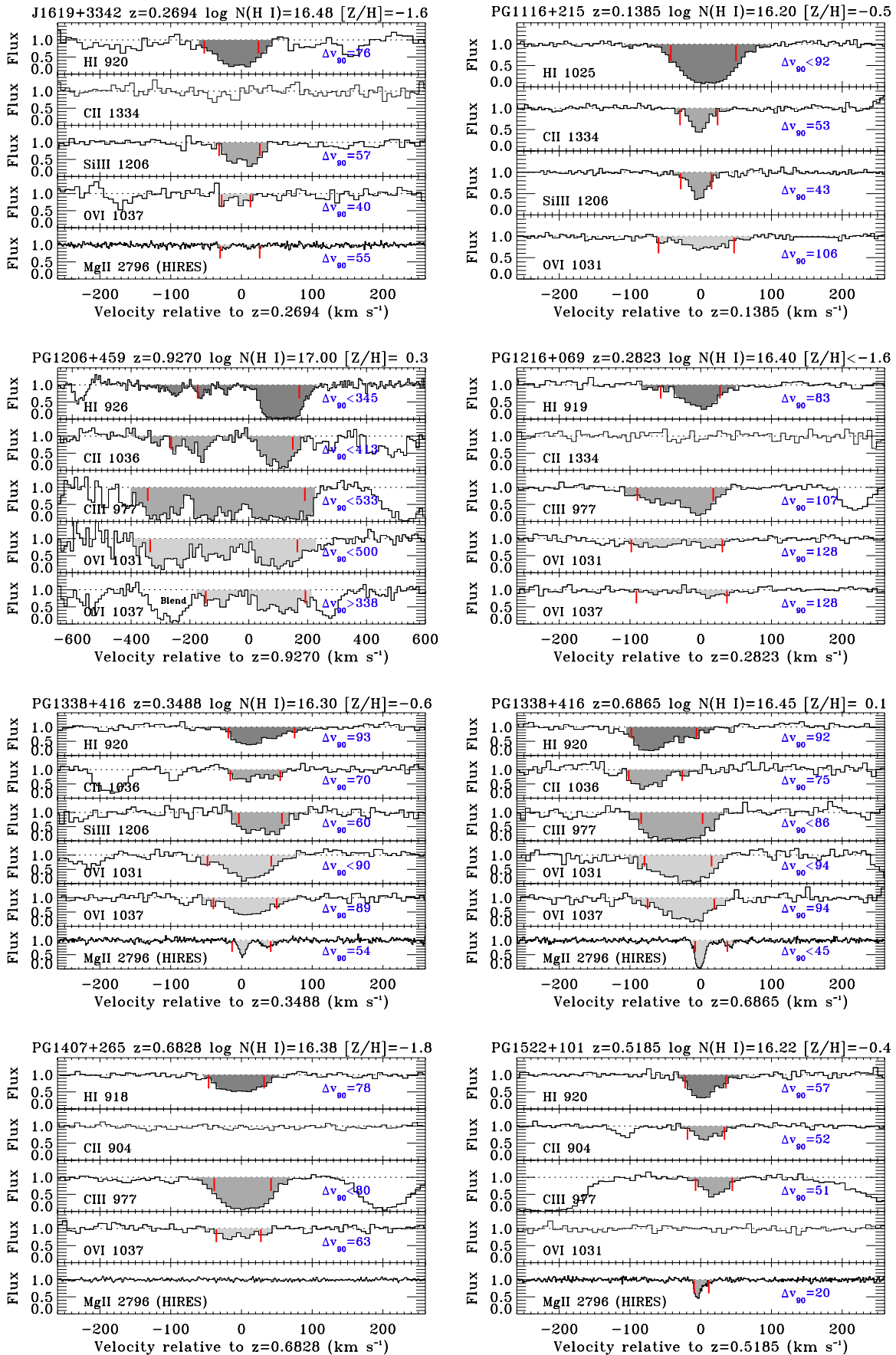(A color version of this figure is available in the online journal.)
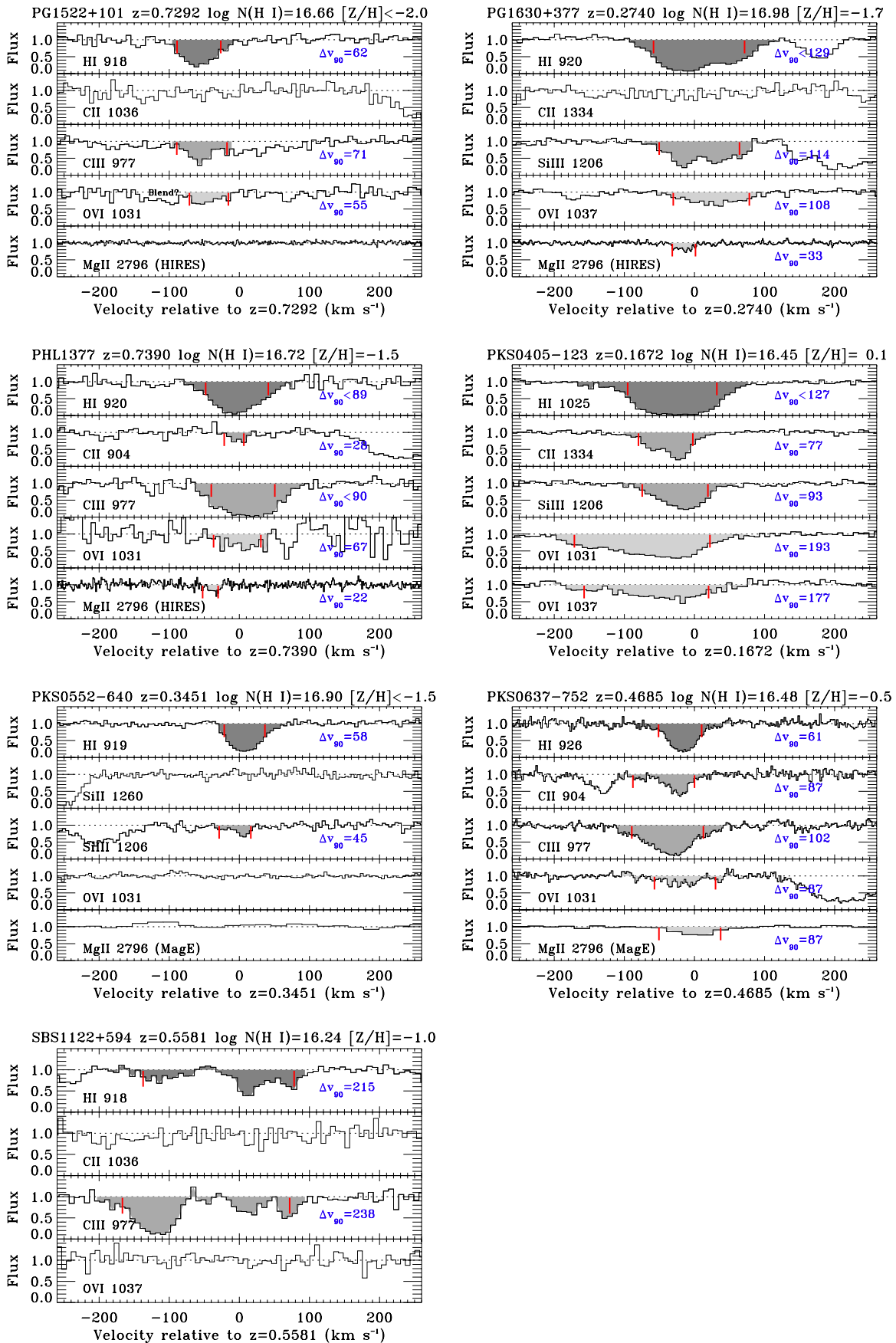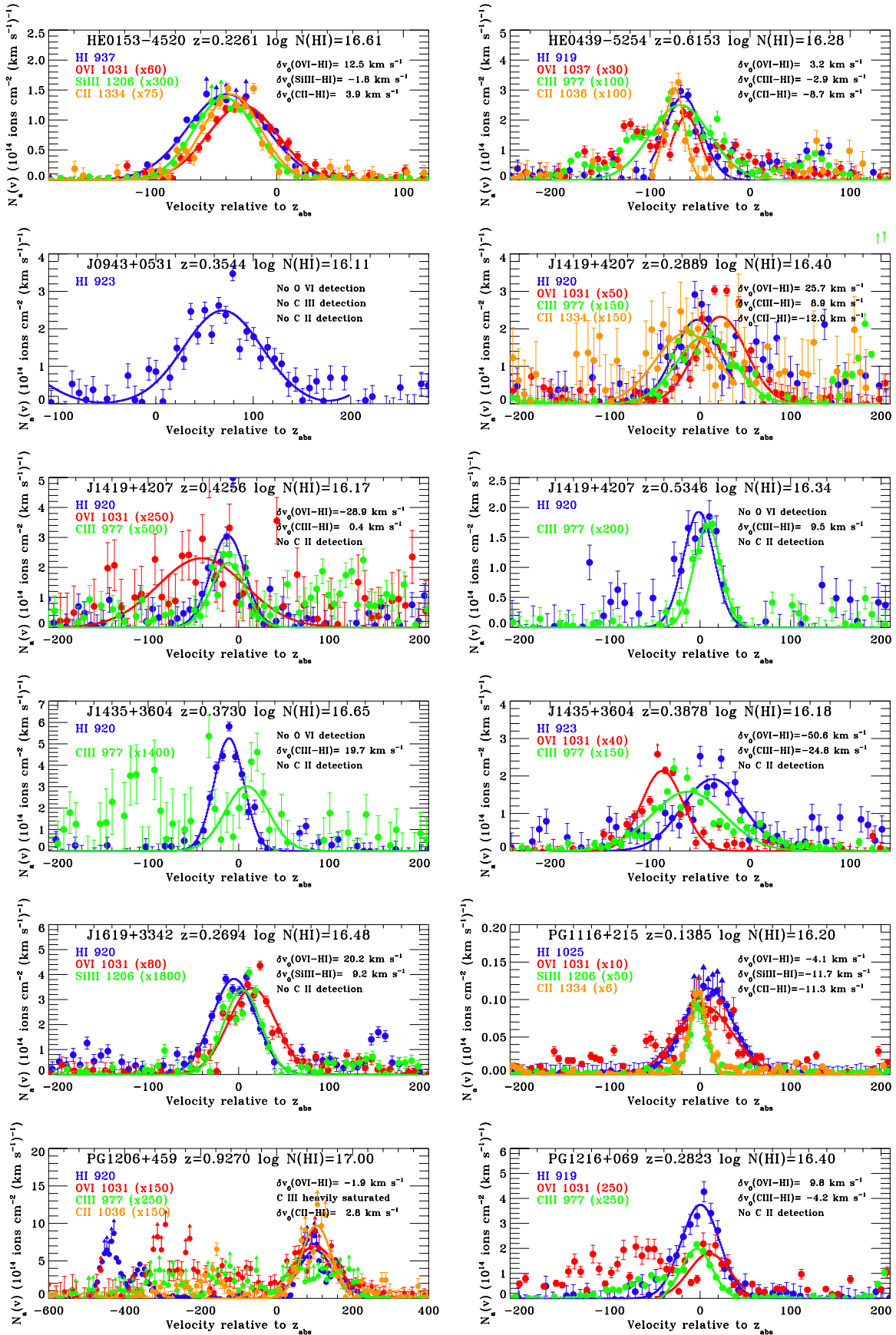
Figure 8. (Continued)

Figure 8. (Continued)

Figure 9. Apparent column density profiles for each LLS in the sample.

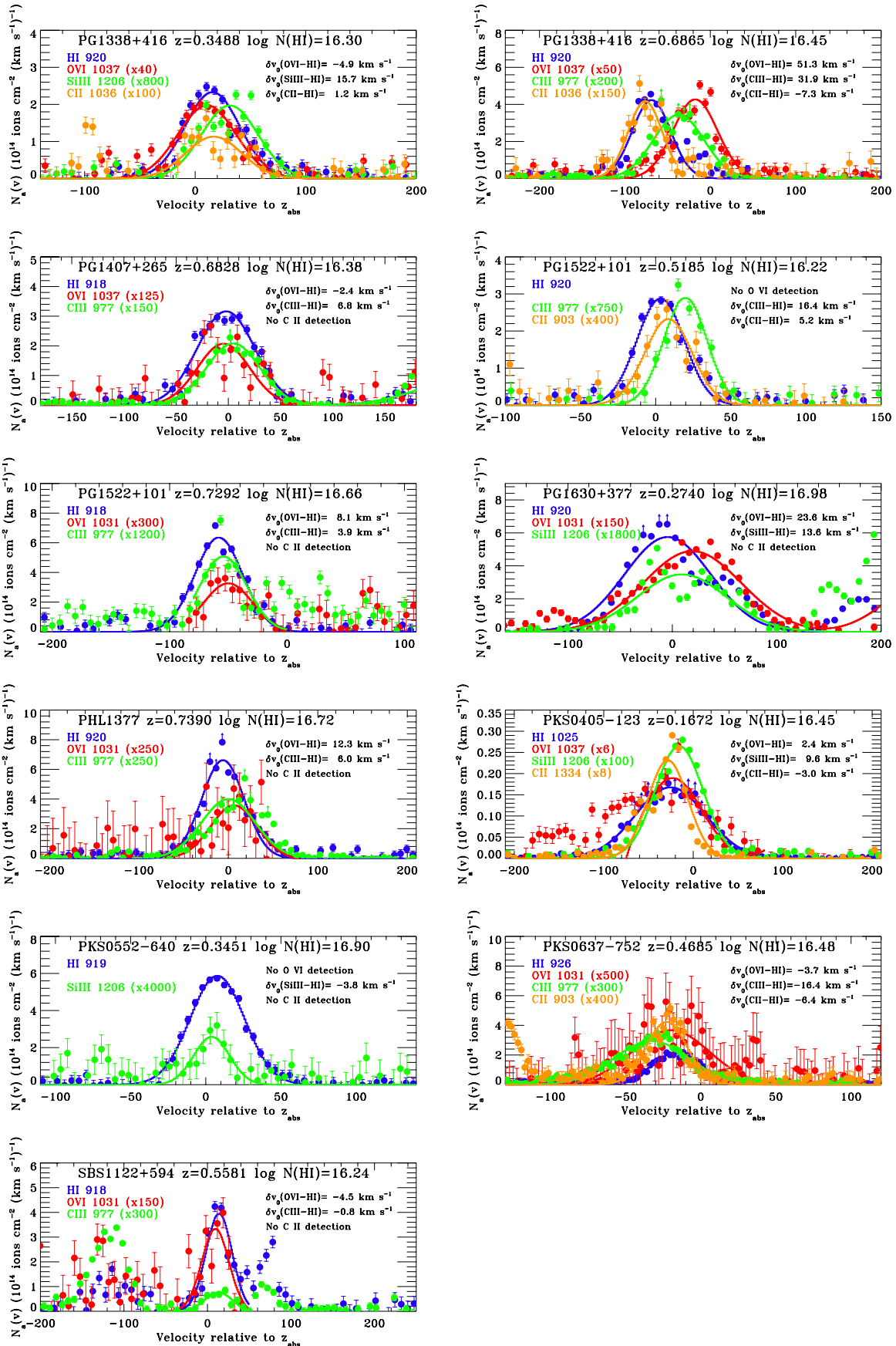(A color version of this figure is available in the online journal.)

Figure 9. (Continued)

intermediate-ion kinematics. However, for O VI, there is a correlation between velocity width and metallicity significant at the 99.0% level. The mean observed velocity widths $\langle \Delta v_{90} \rangle$ are 98 ± 12 km s^{-1} for H I, 65 ± 8 km s^{-1} for C II, 41 ± 8 km s^{-1} for Mg II, 83 ± 14 km s^{-1} for C III, and 97 ± 10 km s^{-1} for O VI. The higher mean line width for O VI than C II reinforces the conclusion that LLSs are generally multiphase systems. The narrowness of the mean C II line width indicates that LLSs are sub-virial objects.

4. We calculate the H$^+$ column in the O VI-bearing gas, under a range of scenarios for how the metallicities in the low-ion and high-ion phases are connected, ranging from the case where the metallicities are the same in each phase (condensation model) to the case where the high-ion phase has solar metallicity (outflow or recycled wind model). *In any of these three cases*, LLSs contain a significant reservoir of highly ionized material, with log N(high-ion H II) ~ 17.6–20, corresponding to a mass M(high-ion) $\sim 10^{8.5-10.9}$ $M_\odot$ out to impact parameters of 150 kpc. This is of similar order to the mass contained in the low-ion phase of LLSs (L13; Werk et al. 2013). Accounting for the O VI phase therefore approximately doubles the contribution of LLSs to the cosmic baryon budget. These results show that *all* LLS-traced CGM, whatever kind of galaxy lies underneath, contains a significant fraction of baryons in its high-ion phase.

APPENDIX

In Figure 8, we present normalized flux profiles of H I, a low ion (C II or Si II), an intermediate ion (C III or Si III), and the high-ion O VI in each LLS. Where Keck/HIRES or Magellan/MagE data exist, we have added the profile of Mg II $\lambda 2796$ or Mg II $\lambda 2803$ to the bottom panel. For H I, a single Lyman series line (unsaturated where possible) is chosen to represent the component structure. For the low ions, either C II $\lambda 903.96$, C II $\lambda 1036$, C II $\lambda 1334$, Si II $\lambda 1020$, or Si II $\lambda 1260$ is shown, using the line that best displays the component structure without saturation. For the intermediate ions, the choice of C III $\lambda 977$ or Si III $\lambda 1206$ depends on redshift or saturation. The systems are ordered alphabetically by target name. The interval between the two red tick marks in each panel indicates the velocity width of absorption Δv_{90}; this value (in km s^{-1}) is annotated on each panel. Gray shading is used when significant absorption ($>3\sigma$) is seen in a given line. Only unblended O VI lines are shown (either $\lambda 1031$, $\lambda 1037$, or both). Further spectral data for some (but not all) of these systems are given in L13. Note that here we adopt the redshifts given to four significant digits in Table 1 of L13; small velocity shifts may be observed between these figures and those shown in L13. This does not affect our kinematic analysis as we are interested in velocity differences. Blends caused by the Lyα forest or other contaminating lines are identified on the plots.

In Figure 9, we compare the apparent column density profiles of H I, C II, C III, and O VI in each LLS. Gaussian fits to

the strongest component of absorption are used to determine the velocity centroid (relative to the systemic redshift of the absorber) of each species. The strongest-component centroid offsets v_0(O VI–H I), v_0(C III–H I), and v_0(C II–H I) are annotated on the panels. The scale factors were selected to normalize the peak of each profile to the same level, for ease of comparison.

REFERENCES

Asplund, M., Greenness, N., Jacques Sauval, A., & Scott, P. 2009, ARA&A, 47, 481
Battisti, A. J., Meiring, J. D., Tripp, T. M., et al. 2012, ApJ, 744, 93
Bergeron, J. 1986, A&A, 155, L8
Bergeron, J., Petitjean, P., Sargent, W. L. W., et al. 1994, ApJ, 436, 33
Bordoloi, R., Lilly, S. J., Hardmeier, E., et al. 2013, ApJ, submitted (arXiv:1307.6553)
Bouché, N., Hohensee, W., Vargas, R., et al. 2012, MNRAS, 426, 801
Bregman, J. 2007, ARA&A, 45, 221
Cen, R., & Chisari, N. E. 2011, ApJ, 731, 11
Chen, H.-W., & Mulchaey, J. S. 2009, ApJ, 701, 1219
Chen, H.-W., & Prochaska, J. X. 2000, ApJL, 543, L9
Churchill, C. W., Kacprzak, G. G., Steidel, C. C., et al. 2012, ApJ, 760, 68
Collins, J. A., Shull, J. M., & Giroux, M. L. 2005, ApJ, 623, 196
Cooksey, K. L., Prochaska, J. X., Chen, H.-W., Mulchaey, J. S., & Weiner, B. J. 2008, ApJ, 676, 262
Crighton, N. H. M., Bechtold, J., Carswell, R. F., et al. 2013a, MNRAS, 433, 178
Crighton, N. H. M., Hennawi, J. F., & Prochaska, J. X. 2013b, ApJL, 776, L18
Davé, R., Finlantor, K., & Oppenheimer, B. D. 2012, MNRAS, 421, 98
Dessauges-Zavadsky, M., Ellison, S. L., & Murphy, M. T. 2009, MNRAS, 396, L61
Ding, J., Charlton, J. C., Churchill, C. W., & Palma, C. 2003, ApJ, 590, 746
Dopita, M. A., & Sutherland, R. S. 1996, ApJS, 102, 161
Faucher-Giguère, C.-A., & Kereš, D. 2011, MNRAS, 412, L118
Ford, A. B., Davé, R., Oppenheimer, B. D., et al. 2014, MNRAS, submitted (arXiv:1309.5951)
Ford, A. B., Oppenheimer, B. D., Davé, R., et al. 2013, MNRAS, 432, 89
Fox, A. J. 2011, ApJ, 730, 58
Fox, A. J., Petitjean, P., Ledoux, C., & Srianand, R. 2007, ApJL, 668, L15
Fox, A. J., Savage, B. D., & Wakker, B. P. 2006, ApJS, 165, 229
Fox, A. J., Wakker, B. P., Savage, B. D., et al. 2005, ApJ, 630, 332
Fumagalli, M., O'Meara, J. M., Prochaska, J. X., & Worseck, G. 2013, ApJ, 775, 78
Fumagalli, M., Prochaska, J. X., Kasen, D., et al. 2011, MNRAS, 418, 1796
Ganguly, R., Sembach, K. R., Tripp, T. M., & Savage, B. D. 2005, ApJ, 157, 251
Gnat, O., & Sternberg, A. 2007, ApJS, 168, 213
Gnat, O., Sternberg, A., & McKee, C. F. 2010, ApJ, 718, 1315
Green, J. C., Froning, C. S., Osterman, S., et al. 2012, ApJ, 744, 60
Haardt, F., & Madau, P. 1996, ApJ, 461, 20
Haehnelt, M. G., Steinmetz, M., & Rauch, M. 1998, ApJ, 495, 647
Hartigan, P., Raymond, J., & Hartmann, L. 1987, ApJ, 316, 323
Heckman, T. M., Norman, C. A., Strickland, D. K., & Sembach, K. R. 2002, ApJ, 577, 691
Holland, S. T., et al. 2012, Cosmic Origins Spectrograph Instrument Handbook, Version 5.0 (Baltimore, MD: STScI)
Howk, J. C., Ribaudo, J. S., Lehner, N., Prochaska, J. X., & Chen, H.-W. 2009, MNRAS, 396, 1875
Hummels, C. B., Bryan, G. L., Smith, B. D., & Turk, M. J. 2013, MNRAS, 430, 1548
Jenkins, E. B., Bowen, D. V., Tripp, T. M., & Sembach, K. R. 2005, ApJ, 623, 767
Joung, M. R., Bryan, G. L., & Putman, M. E. 2012a, ApJ, 745, 1
Joung, M. R., Putman, M. E., Bryan, G. L., Fernández, X., & Peek, J. E. G. 2012b, ApJ, 759, 137
Kacprzak, G. G., Churchill, C. W., Evans, J. L., Murphy, M. T., & Steidel, C. C. 2011, MNRAS, 416, 3118
Kacprzak, G. G., Churchill, C. W., Steidel, C. C., Spitler, L. R., & Holtzman, J. A. 2012, MNRAS, 427, 3029
Keeney, B. A., Stocke, J. T., Rosenberg, J. L., et al. 2013, ApJ, 765, 27
Kereš, D., Katz, N., Fardal, M., Davé, R., & Weinberg, D. H. 2009, MNRAS, 395, 160
Kirkman, D., & Tytler, D. 1997, ApJL, 489, L123
Kirkman, D., & Tytler, D. 1999, ApJL, 512, L5
Kulkarni, V. P., Khare, P., Som, D., et al. 2010, NewA, 15, 735

Kwak, K., Henley, D. B., & Shelton, R. L. 2011, ApJ, 739, 30
Ledoux, C., Petitjean, P., Fynbo, J. P. U., Møller, P., & Srianand, R. 2006, A&A, 457, 71
Lehner, N., & Howk, J. C. 2011, Sci, 334, 955
Lehner, N., Howk, J. C., Thom, C., et al. 2012, MNRAS, 424, 2896
Lehner, N., Howk, J. C., Tripp, T. M., et al. 2013, ApJ, 770, 138 (L13)
Lehner, N., Prochaska, J. X., Kobulnicky, H. A., et al. 2009, ApJ, 694, 734
Maller, A. H., & Bullock, J. S. 2004, MNRAS, 355, 694
Maller, A. H., Prochaska, J. X., Somerville, R. S., & Primack, J. R. 2003, MNRAS, 343, 268
Marasco, A., Marinacci, F., & Fraternali, F. 2013, MNRAS, 433, 1634
Meiring, J. D., Lauroesch, J. T., Kulkarni, V., et al. 2009, MNRAS, 397, 2037
Meiring, J. D., Tripp, T. M., & Prochaska, J. X. 2011, ApJ, 732, 35
Meiring, J. D., Tripp, T. M., Werk, J. K., et al. 2013, ApJ, 767, 49
Mo, H. J., & Miralda-Escudé, J. 1996, ApJ, 469, 589
Morton, D. C. 2003, ApJS, 149, 205
Murante, G., Calabrese, M., De Lucia, G., et al. 2012, ApJL, 749, L34
Neeleman, M., Wolfe, A. M., Prochaska, J. X., & Rafelski, M. 2013, ApJ, 769, 54
Ocvirk, P., Pichon, C., & Teyssier, R. 2008, MNRAS, 390, 1326
O'Meara, J. M., Prochaska, J. X., Worseck, G., Chen, H.-W., & Madau, P. 2013, ApJ, 765, 137
Oppenheimer, B. D., & Davé, R. 2009, MNRAS, 395, 1875
Oppenheimer, B. D., Davé, R., Kereš, D., et al. 2010, MNRAS, 406, 2325
Oppenheimer, B. D., & Schaye, J. 2013, MNRAS, 434, 1043
Prochaska, J., Chen, H.-W., Wolfe, A. M., Dessauges-Zavadsky, M., & Bloom, J. S. 2008, ApJ, 672, 59
Prochaska, J. X., Weiner, B. J., Chen, H.-W., Cooksey, K. L., & Mulchaey, J. S. 2011, ApJS, 193, 28
Prochaska, J. X., Weiner, B. J., Chen, H.-W., & Mulchaey, J. S. 2006, ApJ, 643, 680
Prochaska, J. X., & Wolfe, A. M. 1997, ApJ, 487, 73
Ribaudo, J., Lehner, N., & Howk, J. C. 2011a, ApJ, 736, 42
Ribaudo, J., Lehner, N., Howk, J. C., et al. 2011b, ApJ, 743, 207
Rudie, G. C., Steidel, C. C., Trainor, R. F., et al. 2012, ApJ, 750, 67
Savage, B. D., Narayanan, A., Lehner, N., & Wakker, B. P. 2011, ApJ, 731, 14
Savage, B. D., Narayanan, A., Wakker, B. P., et al. 2010, ApJ, 719, 1526
Savage, B. D., & Sembach, K. R. 1991, ApJ, 379, 245
Savage, B. D., Wakker, B. P., Sembach, K. R., et al. 2003, ApJS, 146, 125
Sembach, K. R., Wakker, B. P., Savage, B. D., et al. 2003, ApJS, 146, 165
Shen, S., Madau, P., Guedes, J., et al. 2013, ApJ, 765, 89
Shull, J. M., Smith, B. D., & Danforth, C. W. 2012, ApJ, 759, 23
Sijacki, D., Vogelsberger, M., Kereš, D., Springel, V., & Hernquist, L. 2012, MNRAS, 424, 2999
Simcoe, R. A., Sargent, W. L. W., & Rauch, M. 2002, ApJ, 578, 737
Smith, B. D., Hallman, E. J., Shull, J. M., & O'Shea, B. W. 2011, ApJ, 731, 6
Springel, V., & Hernquist, L. 2003, MNRAS, 339, 289
Steidel, C. C. 1990, ApJS, 74, 37
Steidel, C. C., Pettini, M., & Hamilton, D. 1995, AJ, 110, 2519
Stewart, K. R., Kaufmann, T., Bullock, J. S., et al. 2011a, ApJL, 735, L1
Stewart, K. R., Kaufmann, T., Bullock, J. S., et al. 2011b, ApJ, 738, 39
Stinson, G. S., Brook, C., Prochaska, J. X., et al. 2012, MNRAS, 425, 1270
Stocke, J. T., Keeney, B. A., & Danforth, C. W. 2010, PASA, 27, 256
Stocke, J. T., Keeney, B. A., Danforth, C. W., et al. 2013, ApJ, 763, 148
Sutherland, R. S., & Dopita, M. A. 1993, ApJS, 88, 253
Tepper-García, T., Richter, P., Schaye, J., et al. 2011, MNRAS, 413, 190
Thom, C., Tumlinson, J., Werk, J. K., et al. 2012, ApJL, 758, L41
Thom, C., Werk, J. K., Tumlinson, J., et al. 2011, ApJ, 736, 1
Tripp, T. M., Jenkins, E. B., Bowen, D. V., et al. 2005, ApJ, 619, 714
Tripp, T. M., Meiring, J. D., Prochaska, J. X., et al. 2011, Sci, 334, 952
Tripp, T. M., Sembach, K. R., Bowen, D. V., et al. 2008, ApJS, 177, 39
Tumlinson, J., Thom, C., Werk, J. K., et al. 2011a, Sci, 334, 948
Tumlinson, J., Thom, C., Werk, J. K., et al. 2013, ApJ, 777, 59
Tumlinson, J., Werk, J. K., Thom, C., et al. 2011b, ApJ, 733, 111
Tytler, D. 1982, ApJ, 321, 49
van de Voort, F., & Schaye, J. 2012, MNRAS, 423, 2991
Verner, D. A., Barthel, P. D., & Tytler, D. 1994, A&AS, 108, 287
Vogelsberger, M., Sijacki, D., Kereš, D., Springel, V., & Hernquist, L. 2012, MNRAS, 425, 3024
Wakker, B. P., & Savage, B. D. 2009, ApJS, 182, 378
Wakker, B. P., Savage, B. D., Fox, A. J., Benjamin, R. A., & Shapiro, P. R. 2012, ApJ, 749, 157
Wakker, B. P., Savage, B. D., Sembach, K. R., et al. 2003, ApJS, 146, 165
Werk, J. K., Prochaska, J. X., Thom, C., et al. 2012, ApJS, 198, 3
Werk, J. K., Prochaska, J. X., Thom, C., et al. 2013, ApJS, 204, 17
Zonak, S. G., Charlton, J. C., Ding, J., & Churchill, C. W. 2004, ApJ, 606, 196